PHYSICS

Distortion-free sampling of ultrabroadband terahertz electric fields by interfacial spin accumulation

Alexander L. Chekhov[1,2]*, Yannic Behovits[1,2], Julius J. F. Heitz[1,2], Maria-Andromachi Syskaki[3], Samridh Jaiswal[3]†, Oliver Gueckstock[1,2], Bruno R. Serrano[1,2], Amon Ruge[1,2], Jana Kredl[4], Martin Wolf[2], Markus Münzenberg[4], Gerhard Jakob[3], Mathias Kläui[3], Tom S. Seifert[1,2], Tobias Kampfrath[1,2]

In spintronics, FM|HM stacks consisting of a ferromagnetic-metal (FM) and a heavy-metal (HM) layer are model systems for spin transport and spin-charge interconversion. To explore their potential as detectors for ultrabroadband terahertz electromagnetic pulses, we measure the transient optical birefringence the terahertz field induces. Notably, the signal component linear in the FM magnetization agrees excellently with the shape of the incident terahertz electric field at 1 to 13 terahertz and beyond. Analysis indicates that the birefringence arises from the terahertz-field–driven spin accumulation at the FM/HM interface through the spin Rashba-Edelstein effect (SREE). Because of spin-momentum locking, the SREE decays by electron momentum relaxation in <10 femtoseconds, substantially faster than a spin-Hall-effect–induced bulk spin accumulation. Our experiment demonstrates straightforward spintronic sampling of intense ultrabroadband terahertz fields with flat amplitude and phase response. Furthermore, it provides temporal signatures of the SREE and can be viewed as a versatile implementation of interface-specific terahertz time-domain spectroscopy.

INTRODUCTION

Spintronics research has led to promising and fascinating concepts for future applications in magnetic information processing based on electron spins (*1*, *2*). A ubiquitous spintronic model system is a FM|HM stack (Fig. 1A) consisting of a ferromagnetic-metal layer (FM) and a heavy-metal layer (HM). Such heterostructures have powerful features for potential applications, but they also come along with fundamental and methodological questions and challenges.

First, FM|HM stacks allow one to study spin transport between FM and HM. An important process is the spin accumulation at the FM/HM interface that results from spin-charge interconversion of an in-plane charge current (Fig. 1B) (*2*). It is essential for magnetic information writing by spin-orbit torques and, consequently, needs to be understood and optimized (*2*). The current-induced spin accumulation has two major contributions, the spin Hall effect (SHE) and the spin Rashba-Edelstein effect (SREE). Their separation is notoriously challenging because both phenomena have identical macroscopic symmetry properties (*2*). Second, the spin accumulation is localized close to the FM/HM interface (*2*) and expected to decay on the femtosecond timescale (*3*). Therefore, it should ideally be interrogated by schemes that are sensitive to buried interfaces and ultrafast.

Third, FM|HM stacks have found application in terahertz photonics as spintronic terahertz emitters (STEs) (*4*–*12*). As seen in Fig. 1A, an optical femtosecond laser pulse drives a spin current from FM to HM, where spin-charge interconversion converts the spin current into an in-plane charge current burst emitting a terahertz electromagnetic pulse. STEs offer attractive features, such as ultrabroadband gap-free emission at 1 to 30 THz (*4*), flexible pump wavelength (*13*, *14*), terahertz polarization control (*15*), and peak fields of the order of 1 MV/cm (*16*). These features suggest that reversal of the STE principle could lead to versatile schemes for the detection of ultrabroadband coherent terahertz electromagnetic pulses. So far, however, only the Zeeman torque of a terahertz magnetic field on the magnetization of a FM (*17*, *18*) has been exploited (*19*, *20*). While the response function of Zeeman torque field sampling has a very simple structure (*19*), its pronounced low-pass characteristics requires longer signal averaging when the sensitivity at higher frequencies needs to be increased.

To spintronically detect broadband terahertz electric rather than magnetic fields, we propose the reciprocal STE approach of Fig. 1B. Here, the terahertz pulse to be measured is incident onto a FM|HM stack. Inside this spintronic terahertz detector (STD), the terahertz electric field $\boldsymbol{E}$ drives an in-plane charge current with density $\boldsymbol{j}$. Because of spin-charge interconversion, $\boldsymbol{j}$ and, thus, $\boldsymbol{E}$ induce a spin accumulation close to the FM/HM interface where inversion symmetry is broken. In the FM, the transient spin accumulation $\Delta\boldsymbol{s}_{\mathrm{FM}}$ can be interrogated by a time-delayed magneto-optic probe pulse, whose polarization plane is rotated by an angle proportional to $\Delta\boldsymbol{s}_{\mathrm{FM}}$ and, thus, $\boldsymbol{E}$.

We emphasize that the scheme of Fig. 1B is also highly interesting for the fundamental and methodological challenges addressed above. First, it may allow us to monitor the ultrafast conversion of a terahertz charge current $\boldsymbol{j}$ into a transient spin accumulation $\Delta\boldsymbol{s}_{\mathrm{FM}}$ and, thus, identify the dominant contribution, i.e., the SHE or SREE, based on their temporal dynamics. Second, as $\Delta\boldsymbol{s}_{\mathrm{FM}}$ relies on the broken inversion symmetry at the FM/HM interface, the resulting optical birefringence may very sensitively report on so far elusive interfacial resonances in the terahertz range.

In this work, we implement the idea of Fig. 1B to detect broadband terahertz electric fields by ultrafast spin accumulation. We find that the optical probe signal odd in the FM magnetization perfectly follows the shape of the incident terahertz electric field. Consequently, upon

[1]Department of Physics, Freie Universität Berlin, 14195 Berlin, Germany. [2]Department of Physical Chemistry, Fritz Haber Institute of the Max Planck Society, 14195 Berlin, Germany. [3]Institute of Physics, Johannes Gutenberg University, 55099 Mainz, Germany. [4]Institute of Physics, Greifswald University, 17489 Greifswald, Germany.
*Corresponding author. Email: a.chekhov@fu-berlin.de
†Present address: Pragmatic Semiconductor, 400 Cambridge Science Park Milton Road, Cambridge CB4 0WH, UK.

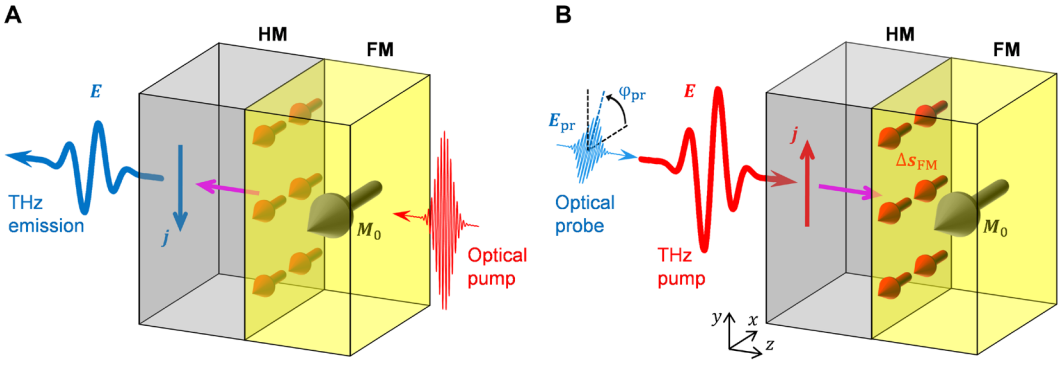

Fig. 1. Spintronic generation and detection of terahertz electric fields. (**A**) In a spintronic THz emitter (STE), an optical pump drives spin transport (magenta arrow) from a ferromagnetic-metal layer FM with equilibrium magnetization $\boldsymbol{M}_0$ into an adjacent heavy-metal layer HM. Through spin-orbit interaction, the spin current is converted into a transverse charge current $\boldsymbol{j}$ that emits a terahertz pulse with electric field $\boldsymbol{E}$. (**B**) A spintronic terahertz detector (STD) is based on reciprocal spintronic terahertz generation. A terahertz electric field $\boldsymbol{E}$ drives an electronic charge current $\boldsymbol{j}$ in a HM|FM stack. Because of spin-orbit interaction, $\boldsymbol{j}$ induces a transient accumulation $\Delta\boldsymbol{s}_{\mathrm{FM}}$ of electron spins in FM, which is monitored by sampling the magnetic linear birefringence (MLB) by a probe pulse with field $\boldsymbol{E}_{\mathrm{pr}}$. Torques on $\boldsymbol{M}_0$ are minimized by choosing $\boldsymbol{E} \perp \boldsymbol{M}_0$.

amplitude calibration, our STD permits straightforward measurement of intense broadband terahertz electric fields with constant detector response amplitude and phase from 1 to 13 THz and beyond.

The quasi-instantaneous temporal response of the STD indicates that the SREE rather than the SHE makes the dominant contribution to the birefringence signal. Our explanation is that the SREE decays within the momentum relaxation time of less than 10 fs owing to spin-momentum locking. In contrast, an SHE-induced spin accumulation in the FM bulk decays substantially more slowly by electron spin relaxation. Our results are an important step toward spintronic terahertz detection and the identification of spin-charge interconversion effects based on their temporal signatures. More generally, our findings indicate that terahertz-pump optical-probe signals odd in $\boldsymbol{E}$ can directly report on the terahertz-field–driven temporal dynamics of spins, electrons, and ions at interfaces. Thus, they open up promising perspectives for interface-specific terahertz time-domain spectroscopy.

RESULTS

Concept

In our approach (Fig. 1B), the terahertz electric field $\boldsymbol{E}$ inside the FM|HM stack induces a spin accumulation close to the FM/HM interface. In layer FM, the transient spin accumulation scales according to $\Delta\boldsymbol{s}_{\mathrm{FM}} \propto \boldsymbol{u}_z \times \boldsymbol{E}$, where $\boldsymbol{u}_z$ is a unit vector along the stack normal (*2*). The $\Delta\boldsymbol{s}_{\mathrm{FM}}$ formally adds to the in-plane magnetization $\boldsymbol{M}_0$ and can be detected by a linearly polarized optical probe pulse (Fig. 1B) through a suitable magneto-optic effect (*21*). Here, we take advantage of magnetic linear birefringence (MLB) that results in a refractive-index change $\propto (\Delta\boldsymbol{s}_{\mathrm{FM}} + \boldsymbol{M}_0)^2$ in the direction parallel to $\boldsymbol{M}_0$. Therefore, we expect an $\boldsymbol{E}$-induced MLB signal

$$S_{\mathrm{MLB}} \propto 2\boldsymbol{M}_0 \cdot \Delta\boldsymbol{s}_{\mathrm{FM}} \tag{1}$$

Note that S_{MLB} is odd in $\boldsymbol{M}_0$ and reports on the spin accumulation $\Delta\boldsymbol{s}_{\mathrm{FM}}$ exclusively in layer FM where $\boldsymbol{M}_0 \neq 0$.

To put this idea on a general basis, we conduct a phenomenological analysis of the expected optical birefringence signal from a FM|HM stack for a perturbing homogeneous electric and magnetic field $\boldsymbol{E}$ and $\boldsymbol{B}$. As shown and discussed in Materials and Methods for normally incident terahertz and probe beams, the signal up to first order in both the FM magnetization $\boldsymbol{M}_0$ and the terahertz field reads

$$S = (a_{\boldsymbol{E}}E + a_{\boldsymbol{B}}B)M_0\cos(2\varphi_{\mathrm{pr}} - \varphi_{\boldsymbol{E}} - \varphi_{\boldsymbol{M}_0}) + (b_{\boldsymbol{E}}E + b_{\boldsymbol{B}}B)M_0\cos(\varphi_{\boldsymbol{E}} - \varphi_{\boldsymbol{M}_0}) \tag{2}$$

Here, E, B, and M_0 are the amplitudes of, respectively, $\boldsymbol{E}$, $\boldsymbol{B}$, and $\boldsymbol{M}_0$, which have in-plane angles of $\varphi_{\boldsymbol{E}}$, $\varphi_{\boldsymbol{E}}+90°$, and $\varphi_{\boldsymbol{M}_0}$ relative to the x axis. In a microscopic interpretation of Eq. 2, the $a_{\boldsymbol{E}}$ term includes the spin accumulation/MLB scenario (Fig. 1B and Eq. 1) with the typical MLB-like dependence on the probe polarization angle φ_{pr}. The $a_{\boldsymbol{B}}$ term shows that the terahertz magnetic field can, in principle, induce an effect with identical angle dependence.

The $b_{\boldsymbol{E}}$ and $b_{\boldsymbol{B}}$ terms capture such effects as spin-orbit torque (*22*) and Zeeman torque (*17*–*20*), respectively. They are detected by magnetic circular birefringence (MCB; Faraday effect), which is independent of φ_{pr} (*23*). Because the sample is isotropic about the surface normal for vanishing $\boldsymbol{E}$, $\boldsymbol{B}$, and $\boldsymbol{M}_0$, the signal S of Eq. 2 depends on φ_{pr} only relative to $\varphi_{\boldsymbol{E}}$ and $\varphi_{\boldsymbol{M}_0}$. For the sake of simplicity, an integration over the whole sample thickness along z (Fig. 1B) is omitted in Eqs. 1 and 2. Likewise, the fields $\boldsymbol{E}$ and $\boldsymbol{B}$ are assumed to be quasi-static.

Experiment

In our setup (Fig. 1B and Materials and Methods), we focus on a potential spin accumulation signal. Consequently, we minimize torque effects ($b_{\boldsymbol{E}}$, $b_{\boldsymbol{B}}$ terms in Eq. 2) by choosing $\varphi_{\boldsymbol{E}} = \varphi_{\boldsymbol{M}_0} \pm 90°$ ($\boldsymbol{E} \perp \boldsymbol{M}_0$), which is achieved with high accuracy by using a reference sample that only exhibits Zeeman torque (*19*). Furthermore, we maximize the $a_{\boldsymbol{E}}$, $a_{\boldsymbol{B}}$ terms by setting $\varphi_{\mathrm{pr}} = \varphi_{\boldsymbol{M}_0} + 45°$, if not mentioned otherwise. The FM magnetization angle is set to $\varphi_{\boldsymbol{M}_0} = 0°$. To cover the large bandwidth from 0.1 to 10 THz and beyond, the terahertz pulse is generated by a large-area STE (peak field >1 MV/cm) (*16*), and the probe pulse (center wavelength, 800 nm) has a duration of 16 fs. To faithfully measure the incident terahertz electric field, Zeeman torque sampling is used (*19*). Once the probe beam has traversed the sample, we detect both its transient rotation and ellipticity.

Our samples are FM(3 nm)|HM(3 nm) metal stacks on glass substrates (see Materials and Methods). They are characterized by

terahertz emission (Fig. 1A) and terahertz transmission spectroscopy (fig. S1). We focus on $Co_{20}Fe_{60}B_{20}$ (CFB) for FM and Pt for HM.

Raw data

Figure 2A shows typical signal waveforms $S(t, \pm\boldsymbol{E}, \pm\boldsymbol{M}_0)$ as obtained from CFB|Pt for opposite directions $\pm\boldsymbol{E}$ of the terahertz electric field and, thus, magnetic field, and opposite directions $\pm\boldsymbol{M}_0$ of the FM magnetization. The signals $S(t, \pm\boldsymbol{E}, +\boldsymbol{M}_0)$ and $S(t, \mp\boldsymbol{E}, -\boldsymbol{M}_0)$ agree excellently. Therefore, it does not matter whether the terahertz field $\boldsymbol{E}$ or the FM magnetization $\boldsymbol{M}_0$ is reversed, in line with Eq. 2. Accordingly, Fig. 2B displays the signal components

$$S_{\pm}(t) = \frac{S(t, \boldsymbol{E}, +\boldsymbol{M}_0) \pm S(t, \boldsymbol{E}, -\boldsymbol{M}_0)}{2} \quad (3)$$

even (S_+) and odd (S_-) in $\boldsymbol{M}_0$. The signal $S_+(t)$ is unipolar, whereas $S_-(t)$ is bipolar and has an approximately vanishing time integral (Fig. 2B). $S_-(t)$ is not only odd in $\boldsymbol{M}_0$ but also in $\boldsymbol{E}$, consistent with Fig. 1A and Eq. 2.

We confirm that S_+ and S_- scale quadratically and linearly with the pump field $\boldsymbol{E}$, respectively (see fig. S2). In the following, we focus on $S_-(t)$ as measured by the probe polarization rotation, which strongly exceeds the probe ellipticity change (fig. S3).

Signal symmetries

In Fig. 2C and fig. S4, we vary the probe polarization angle φ_{pr}. The amplitude of S_- (Fig. 2C) follows a $\sin(2\varphi_{pr})$ dependence, as predicted by Eq. 2 with $\varphi_{\boldsymbol{M}_0} = 0°$ and $\varphi_{\boldsymbol{E}} = 90°$. Therefore, the signal S_- is dominated by the $a_{\boldsymbol{E}}$, $a_{\boldsymbol{B}}$ terms in Eq. 2, consistent with a MLB-type probe mechanism.

To see whether the terahertz electric ($a_{\boldsymbol{E}}$) or magnetic ($a_{\boldsymbol{B}}$) field is responsible for signal S_-, we note that a nonvanishing $a_{\boldsymbol{E}}$ in Eq. 2 requires broken inversion symmetry of the FM|HM stack, whereas $a_{\boldsymbol{B}}$ does not (see Materials and Methods). More precisely, $a_{\boldsymbol{E}}$ turns into $-a_{\boldsymbol{E}}$ for a perfectly reversed stack HM|FM, whereas $a_{\boldsymbol{B}}$ does not change sign.

As seen in Fig. 3A, the signal $S_-(t)$ from CFB(3 nm)|Pt(3 nm) equals the signal from Pt(3 nm)|CFB(3 nm) times − 0.84 (fig. S5). This nearly complete signal reversal indicates that $S_-(t)$ arises from the electric rather than the magnetic component of the terahertz field averaged over the sample thickness, i.e., $|a_{\boldsymbol{E}}| \gg |a_{\boldsymbol{B}}|$. We ascribe the deviation from a full signal reversal to the fact that CFB|Pt and the reversely grown Pt|CFB stacks are imperfect mirror versions of each other. One reason can be a different structure of the CFB/Pt and Pt/CFB interface (*24*).

For comparison, Fig. 3B displays terahertz emission signals odd in $\boldsymbol{M}_0$ from the same samples. The opposite sign of the signals from CFB|Pt and Pt|CFB indicates that spintronic terahertz emission (Fig. 1A), just like terahertz-field–induced MLB (Figs. 1B and 3A), is governed by the broken inversion symmetry of the sample.

Dynamic response

To summarize, the signal $S_-(t)$ depends linearly on the terahertz electric field $\boldsymbol{E}(t)$. Therefore, it can be used to sample $\boldsymbol{E}(t)$ with the CFB|Pt stack acting as a STD. Note that Eq. 2 refers to quasi-static fields $\boldsymbol{E}$ and $\boldsymbol{B}$. In the case of a time-dependent incident linearly polarized field $\boldsymbol{E}_{inc}(t)$, $a_{\boldsymbol{B}} = 0$ and optimum detection configuration ($\varphi_{\boldsymbol{M}_0} = 0°$, $\varphi_{\boldsymbol{E}} = 90°$, and $\varphi_{pr} = 45°$), Eq. 2 can be substituted by

$$S_-(t) = (H * E_{inc})(t) \quad (4)$$

Here, $(H * E_{inc})(t) = \int dt' H(t-t') E_{inc}(t')$ denotes convolution of the terahertz electric-field amplitude $E_{inc}(t)$ along $\varphi_{\boldsymbol{E}}$ and the response function $H(t)$ of the STD, which scales with $a_{\boldsymbol{E}} M_0$. To obtain a signal $S_-(t)$ that is as close to $E_{inc}(t)$ as possible, $H(t)$ should be proportional to Dirac's $\delta(t)$ function. In other words, the ideal response should be instantaneous and yield $S_-(t) \propto E_{inc}(t)$.

To determine $H(t)$, Fig. 4A compares the measured $S_-(t)$ to the incident terahertz electric field $E_{inc}(t)$ obtained by Zeeman-torque sampling (see Materials and Methods and fig. S6). We find that the scaled signals agree perfectly with each other, and we have $S_-(t) \propto E_{inc}(t)$. Likewise, the Fourier amplitudes $|\widetilde{S}_-(\omega)|$ and $|\widetilde{E}_{inc}(\omega)|$ of the two signals excellently agree over the full range of frequencies $\omega / 2\pi$ from 1 to 13 THz (Fig. 4B).

For a more quantitative treatment, we Fourier-transform Eq. 4 and calculate the Fourier-transformed $H(t)$ by $\widetilde{H}(\omega) = \widetilde{S}_-(\omega) / \widetilde{E}_{inc}(\omega)$. As seen in Fig. 4C, the amplitude and phase of $\widetilde{H}(\omega)$ are constant over the entire range of 1 to 13 THz of our experiment. To estimate the response time τ_H of the STD, we assume that $H(t)$ follows a single-sided exponential with time constant τ_H, resulting in

$$\widetilde{H}(\omega) \propto \frac{1}{1 + i\omega\tau_H} \quad (5)$$

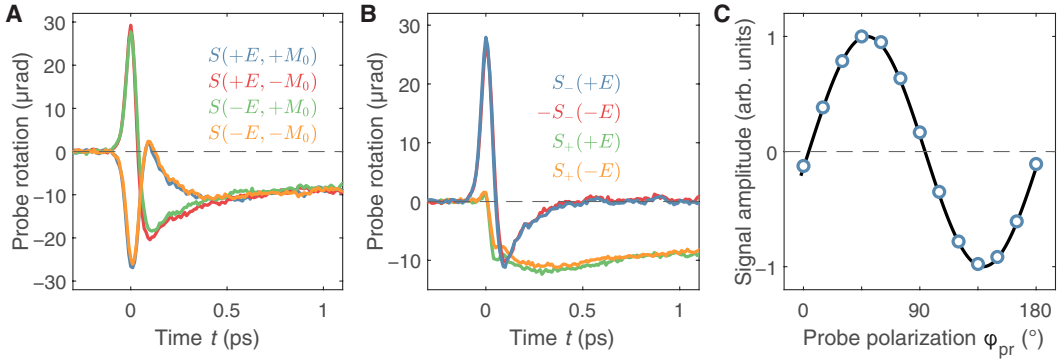

Fig. 2. Typical birefringence signals from a CFB(3 nm)|Pt(3 nm) stack. (**A**) Signal waveforms $S(t, \pm\boldsymbol{E}, \boldsymbol{M}_0)$ and $S(t, \boldsymbol{E}, \pm\boldsymbol{M}_0)$ for opposite polarities $\pm\boldsymbol{E}$ of the terahertz pump field and opposite magnetizations $\pm\boldsymbol{M}_0$. Note that curves are plotted on top of each other. (**B**) Signal waveforms $S_{\pm}(t)$ odd and even with respect to $\boldsymbol{M}_0$ (see Eq. 3), each shown for opposite terahertz pump fields $\pm\boldsymbol{E}$. (**C**) Amplitude of the signal $S_-(t)$ versus probe polarization angle φ_{pr}. A fit by $\sin(2\varphi_{pr} - 2\varphi_0)$ (black line) indicates a slight miscalibration of the probe polarization angle by $\varphi_0 = 4°$. Error bars are smaller than the symbol size.

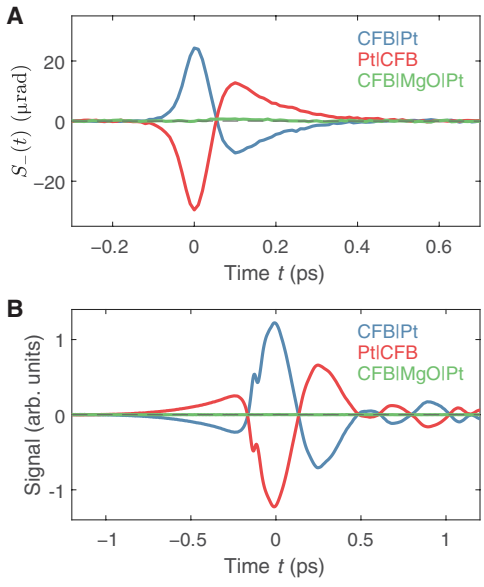

Fig. 3. Impact of sample structure. (**A**) Birefringence signals $S_-(t)$ (Fig. 1B) and (**B**) terahertz emission signals (Fig. 1A) from stacks CFB|Pt (blue lines), Pt|CFB (red), and CFB|MgO|Pt (green). Each layer in each stack is 3 nm thick.

in the frequency domain. The calculated $|\widetilde{H}(\omega)|$ curves for $\tau_H = 5$ fs and 100 fs in Fig. 4C indicate that τ_H is not substantially larger than 5 fs.

We conclude that the MLB-type signal $S_-(t)$ directly provides the time-dependent terahertz electric field $E_{\mathrm{inc}}(t)$ incident on the CFB|Pt stack. The absolute field amplitude can straightforwardly be determined by a calibration measurement using, e.g., Zeeman torque sampling (fig. S6) (*19*).

DISCUSSION

STD features

Our STD CFB|Pt is highly useful for the distortion-free determination of the terahertz electromagnetic field of intense linearly polarized terahertz pulses used in nonlinear terahertz spectroscopy (*17*, *18*, *22*, *23*, *25*–*33*). Notably, the STD offers both a constant transfer function $\widetilde{H}(\omega)$ over an ultrabroad bandwidth of 1 to 13 THz and a high amplitude linearity, in contrast to electro-optic crystals, such as ZnTe and GaP (*25*), which also require nontrivial deconvolution procedures (fig. S6) (*19*, *34*). For reliable determination of $E_{\mathrm{inc}}(t)$, reversal of the STD magnetization $\boldsymbol{M}_0$ is sufficient (Fig. 2B).

The detector response magnitude $|\widetilde{H}(\omega)|$ of the current STD is comparable to that of the recently demonstrated Zeeman-torque detector (ZTD) at about 8 THz but does not require noise-prone post-differentiation of the measured signal. For example, measurement of the $E(t)$ traces in Fig. 4A by the ZTD took a factor of 2.5 more time than by the STD. However, $|\widetilde{H}(\omega)|$ is about three orders of magnitude smaller than that of a 50-μm-thick GaP(110) broadband electro-optic detector (*34*, *35*). We emphasize that the reduced sensitivity is no issue for detecting the intense pulses used in nonlinear terahertz spectroscopy. Similar to STEs (*5*), the STD approach has large potential to reach or exceed the sensitivity of electro-optic detectors because it offers a large number of parameters for optimization. Examples include the FM and HM materials, thickness and sequence of the constituting layers, as well as coatings and in-plane microstructuring.

In addition to its flat broadband response function, the STD has further attractive features. It can easily be included in any existing electro-optic sampling setup with minimum changes, i.e., by just substituting the electro-optic detection crystal by the STD and setting the probe polarization to 45°. In the case of a terahertz pulse with elliptical or even arbitrary polarization, its two orthogonal electric field components can be sampled by using a linear polarizer as analyzer before the STD. Last, the interaction length between terahertz pulse and optical probe pulse is constrained to the FM/HM interface. Therefore, a STD can be used to sample terahertz electric fields with a longitudinal resolution in the nanometer range.

Detection mechanism

The observed ultrabroadband signal contribution $S_- \propto a_E M_0 E$ in Eq. 2 can, in principle, be induced by many processes. An example is a pump-induced magnetization change $\Delta\boldsymbol{M} = \boldsymbol{M} - \boldsymbol{M}_0$ due, for instance, to a spin accumulation $\Delta\boldsymbol{s}_{\mathrm{FM}}$ (Fig. 1B). On the other hand, the MLB-like S_- may also originate from changes in the non-spin degrees of freedom of the sample, although $\Delta\boldsymbol{M} = 0$ (*23*). However, additional data and arguments indicate that such nonmagnetic effects make a minor contribution to our signals S_- (fig. S3). Therefore, S_- arises from an in-plane magnetization change $\Delta\boldsymbol{M}$ and its detection through MLB according to $S_- \propto \Delta(\boldsymbol{M}^2) \approx 2\boldsymbol{M}_0 \cdot \Delta\boldsymbol{M}$ (see Materials and Methods). As a consequence, $\Delta\boldsymbol{M}$ contributes to S_- only in regions with nonvanishing static magnetization $\boldsymbol{M}_0$, i.e., in the FM bulk and at the FM/HM interface.

To reveal the origin of these $\Delta\boldsymbol{M}$ components, we introduce a MgO layer between FM = CFB and HM = Pt. The insulating MgO greatly suppresses electron spin transport between FM and HM, as confirmed by terahertz emission spectroscopy (Figs. 1A and 3B). As seen in Fig. 3A, the MgO also quenches the MLB signal S_-. This notable result implies that the FM/HM interface must be sufficiently conductive to achieve a sizeable magnetization change $\Delta\boldsymbol{M} \propto S_-$ in FM. It indicates that $\Delta\boldsymbol{M}$ arises from spin transport between HM and FM and, therefore, equals the resulting spin accumulation $\Delta\boldsymbol{s}_{\mathrm{FM}}$. This conclusion is fully consistent with the scenario outlined by Fig. 1B and Eq. 1.

At least two microscopic mechanisms are known to contribute to $\Delta\boldsymbol{s}_{\mathrm{FM}}$: the SHE and the SREE (*2*). The SHE converts the in-plane bulk charge current $\boldsymbol{j}$ into an out-of-plane spin current that accumulates in the FM and HM. In contrast, the SREE relies on spin-momentum locking of electronic states at the FM/HM interface, where inversion symmetry is broken. Consequently, an interfacial spin accumulation appears whenever an in-plane charge current is flowing.

The experimental separation of SHE and SREE is a longstanding challenge in spintronics research because the two effects have identical macroscopic symmetry properties and the spatial localization of the induced spin accumulation at the FM/HM interface is quite similar (*2*). However, we expect that the relaxation time of the SHE-induced spin accumulation $\Delta\boldsymbol{s}_{\mathrm{FM}} \parallel \boldsymbol{M}_0$ in the FM bulk is given by the spin-electron relaxation time of the FM material, which amounts to ≈ 100 fs for CFB (*3*). As seen in Fig. 3C, $\tau_H = 100$ fs is highly inconsistent with the measured STD response H. In contrast, the decay of the SREE-related spin accumulation is, owing to spin-momentum locking, determined by the momentum relaxation time of the electrons. The latter is smaller than 10 fs in thin-film stacks (*36*, *37*) like ours (see fig. S1) and consistent with the response time $\tau_H \lesssim 5$ fs of the STD (see Fig. 4C and Eq. 5).

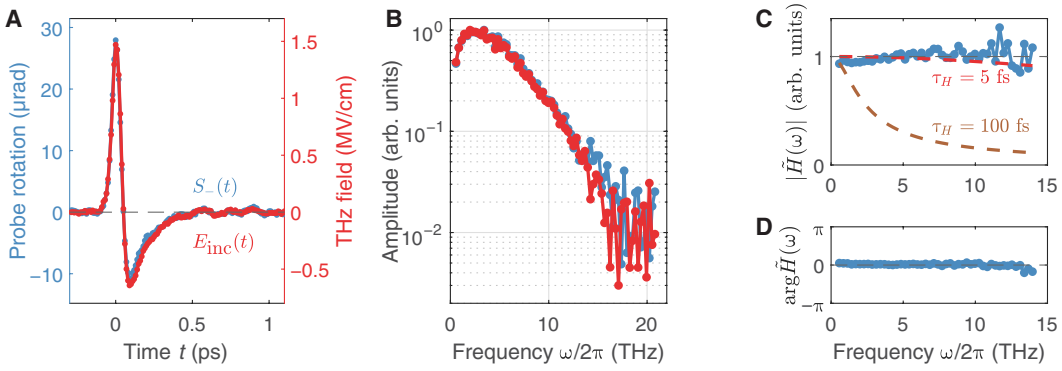

Fig. 4. Dynamic response of the STD. (**A**) Birefringence signal $S_-(t)$ (blue line) from CFB(3 nm)|Pt(3 nm) in comparison to the incident terahertz electric field $E_{inc}(t)$ (red). (**B**) Fourier amplitudes $|\widetilde{S}_-(\omega)|$ and $|\widetilde{E}_{inc}(\omega)|$ of the signals of (A) versus frequency ω/2π. (**C**) Amplitude and (**D**) phase of the resulting transfer function $\widetilde{H}(\omega) = \widetilde{S}_-(\omega)/\widetilde{E}_{inc}(\omega)$. Dashed lines are calculated $\widetilde{H}(\omega)$ using Eq. 5 for a relaxation time τ_H of 5 and 100 fs, which can be interpreted as lifetime of the spin accumulation in layer FM (Fig. 1B).

We summarize that the STD signal S_- (Fig. 3A) can consistently be assigned to (i) an interfacial spin accumulation induced by the terahertz electric field and the SREE and (ii) its MLB-type magneto-optic probing (Fig. 1B and Eq. 1). This interpretation is confirmed by measurements of S_- (Fig. 1B) and terahertz emission spectroscopy (Fig. 1A) on more FM|HM stacks made of various metals (figs. S1 and S5).

Toward terahertz interface spectroscopy

The signal S_- arises from a pump-induced change $\Delta\boldsymbol{E}_{pr}$ in the transmitted probe field $\boldsymbol{E}_{pr}$ (Fig. 1B). Analogous to electro-optic sampling (*34*, *35*), $\Delta\boldsymbol{E}_{pr}$ scales with the product of $\boldsymbol{E}_{pr}$ and the terahertz field $\boldsymbol{E}$ (fig. S2). Therefore, it is the result of a second-order nonlinear effect, which is typically quantified by the second-order optical susceptibility tensor $\chi^{(2)}$ (see Materials and Methods). Because a nonzero $\chi^{(2)}$ requires a locally broken inversion symmetry, $\chi^{(2)}$ is often highly interface-sensitive. The very different amplitudes of the birefringence signal S_- from samples with and without MgO interlayer (Fig. 3A) confirm the interface sensitivity of our approach.

At infrared frequencies $\omega/2\pi > 30$ THz, an interfacial $\chi^{(2)}(\omega)$ can routinely be probed in the frequency domain by infrared-visible sum frequency generation (SFG) spectroscopy (*38*). This technique has provided unique information on the properties of, e.g., interfacial water due to resonant coupling of the infrared wave to intramolecular vibrations (*39*). So far, however, access to $\chi^{(2)}$ at frequencies $\omega/2\pi < 30$ THz by noncollinear SFG has been hampered by the relatively small frequency of terahertz waves, which makes the spectral and spatial separation of the SFG signal difficult (*40*).

This constraint does not apply to our straightforward collinear terahertz-pump optical-probe experiment, which operates fully in the time domain (Fig. 1B). It allows us to extract a response function $\widetilde{H}(\omega)$ (Eq. 4) that is proportional to the complex-valued elements of $\chi^{(2)}(\omega)$ of the CFB/Pt interface and at terahertz frequencies. We expect that such intrinsically phase-sensitive time-domain probing of $\chi^{(2)}(\omega)$ can be applied to any interface, potentially thereby yielding unprecedented insights into the numerous terahertz resonances of interfaces in condensed matter. Examples include intermolecular modes of interfacial water (*41*), a two-dimensional electron gas between two insulating solids (*42*), or the dynamics of interfacial spin-charge interconversion, as addressed here.

Future directions

The preceding discussion implies that our results are relevant from at least three perspectives. First, from an applied viewpoint, the STD demonstrated here has an ideal response function and directly delivers the incident instantaneous terahertz electric field without any distortion at 1 to 13 THz and likely far beyond. The upper frequency is currently given by the maximum frequency of our high-field terahertz source (*16*, *19*). However, the detector bandwidth (Eqs. 4 and 5) is only limited by the electron momentum-relaxation time $\tau_H \lesssim 5$ fs and suggests that $|\widetilde{H}(\omega)/\widetilde{H}(0)|$ drops below 50% above a frequency of $1/2\pi\tau_H \gtrsim 30$ THz. We expect that the detector sensitivity can be increased considerably by the well-developed spintronics toolbox for material and interface engineering.

Second, from a fundamental viewpoint, our broadband terahertz-pump magneto-optic-probe experiment provides a direct temporal signature of the SREE. It, thus, demonstrates a time-domain strategy to differentiate contributions from the SREE and SHE, which are typically hard to separate with other techniques. Such separation will enable a better understanding of spin-charge interconversion in FM|HM stacks, which is important to optimize applications, like spin-orbit torque and spintronic terahertz-field detection. We further expect that our methodology will provide insights into the elementary steps of electric-field–induced spin accumulation in a wide range of environments. Examples include the surface states of three-dimensional topological insulators (*43*), the bulk of magnetic materials whose inversion symmetry is broken on the unit-cell level (*44*), and chiral Weyl semimetals that host parallel rather than the SREE-like perpendicular spin-momentum locking (*45*).

Last, from a methodological viewpoint, our time-domain measurement of the response function $\widetilde{H}(\omega)$ (Eq. 4) provides direct access to the quadratic susceptibility $\chi^{(2)}(\omega)$ of the FM/HM interface at terahertz frequencies $\omega/2\pi$. In this sense, our experiment can be considered an important step toward sensitive probing of the plethora of interfacial resonances in the elusive terahertz range, including spin dynamics, electronic currents, and molecular vibrations.

MATERIALS AND METHODS

Signal phenomenology

For a linearly polarized probe beam that is normally incident onto the FM|HM sample stack along the z axis (Fig. 1B), the

sample-induced rotation or ellipticity of the probe polarization is given by (*23*)

$$S \propto |\boldsymbol{E}_{\mathrm{pr0}}|^2 \left[\frac{\sigma_{yy}-\sigma_{xx}}{2} \sin\left(2\varphi_{\mathrm{pr}}\right) + \frac{\sigma_{yx}+\sigma_{xy}}{2} \cos\left(2\varphi_{\mathrm{pr}}\right) + \frac{\sigma_{yx}-\sigma_{xy}}{2} \right] \tag{6}$$

Here, $\boldsymbol{E}_{\mathrm{pr0}}$ is the probe electric field amplitude in the frequency domain, and the σ_{ij} with $i, j = x$ or y are the in-plane components of the conductivity tensor at the probe frequency. In Eq. 6, the integration over the probed sample volume and over all probe frequencies is omitted for simplicity.

As discussed previously (*23*), one can consider the impact of the pump fields $\boldsymbol{E}$ and $\boldsymbol{B}$ on the sample (Fig. 1B) explicitly or implicitly. In the explicit treatment, we quantify directly how $\boldsymbol{E}$ and $\boldsymbol{B}$ modify the linear optical response σ_{ij} of the sample. This treatment is highly relevant for terahertz field detection where we wish to infer $\boldsymbol{E}$ from the measured signal S. In the implicit treatment, we consider how $\boldsymbol{E}$ and $\boldsymbol{B}$ modify each degree of freedom of the sample, all of which determine the optical response σ_{ij}.

Explicit pump treatment

In the absence of the static magnetization $\boldsymbol{M}_0$ and homogeneous electric and magnetic fields $\boldsymbol{E}$ and $\boldsymbol{B}$, respectively, our FM|HM sample stacks are isotropic in the stack plane but exhibit broken inversion symmetry along the out-of-plane direction. Therefore, the spatial point symmetries of our samples for vanishing $\boldsymbol{M}_0$, $\boldsymbol{E}$, and $\boldsymbol{B}$ are summarized by the point group ∞m.

Up to second order in quasi-static observables $\boldsymbol{M}_0$, $\boldsymbol{E}$, and $\boldsymbol{B}$, the conductivity tensor has the structure

$$\sigma_{ij} = \sigma_{ij}\left(\boldsymbol{M}_0, \boldsymbol{E}, \boldsymbol{B}\right) = \sigma_{0ij} + \sum \alpha_{ijkl} M_{0k} E_l + \sum \beta_{ijkl} M_{0k} B_l + \sum \gamma_{ijkl} E_k E_l \tag{7}$$

Here, σ_{0ij} is the isotropic optical conductivity in the absence of $\boldsymbol{M}_0$, $\boldsymbol{E}$, and $\boldsymbol{B}$. The coefficients α_{ijkl}, β_{ijkl}, and γ_{ijkl} are fourth-order tensors, and the contribution quadratic in $\boldsymbol{B}$ is neglected. By applying the symmetry operations of the sample's point group, we identify the nonzero elements of each of the three fourth-order tensors and relationships between them. After applying trigonometric relationships, we arrive at

$$\begin{aligned} S = {} & \left(a_{\boldsymbol{E}} E + a_{\boldsymbol{B}} B\right) M_0 \cos\left(2\varphi_{\mathrm{pr}} - \varphi_{\boldsymbol{E}} - \varphi_{\boldsymbol{M}_0}\right) \\ & + \left(b_{\boldsymbol{E}} E + b_{\boldsymbol{B}} B\right) M_0 \cos\left(\varphi_{\boldsymbol{E}} - \varphi_{\boldsymbol{M}_0}\right) + c_{\boldsymbol{E}} E^2 \cos\left(2\varphi_{\mathrm{pr}} - 2\varphi_{\boldsymbol{E}}\right) \end{aligned} \tag{8}$$

Here, E, B, and M_0 are the in-plane amplitudes of, respectively, $\boldsymbol{E}$, $\boldsymbol{B}$, and $\boldsymbol{M}_0$, which have in-plane angles of $\varphi_{\boldsymbol{E}}$, $\varphi_{\boldsymbol{E}} + 90°$, and $\varphi_{\boldsymbol{M}_0}$ relative to the x axis. Furthermore, $2a_{\boldsymbol{E}} = -\alpha_{xyyy} - \alpha_{yxyy}$, $2a_{\boldsymbol{B}} = \beta_{yyyy} - \beta_{xxyy}$, $b_{\boldsymbol{E}} = \alpha_{yxyy} - \alpha_{xyyy}$, $b_{\boldsymbol{B}} = \beta_{yyyy} - \beta_{xxyy} - 2\beta_{xyxy}$, and $c_{\boldsymbol{E}} = \gamma_{yyyy} - \gamma_{xxyy}$.

As the tensor α_{ijkl} is of fourth order and axial, space inversion will result in a transformed tensor $-\alpha_{ijkl}$ and, thus, a sign change of $a_{\boldsymbol{E}}$ and $b_{\boldsymbol{E}}$. This conclusion remains valid for spatial reflection at the FM/HM interface plane because our FM|HM stack is in-plane isotropic for $\boldsymbol{M}_0 = 0$.

Relationship to $\chi^{(2)}$

In Eq. 7, the change $\sum \alpha_{ijkl} M_{0k} E_l$ in the optical conductivity implies that the optical probe field $\boldsymbol{E}_{\mathrm{pr0}}$ induces an additional optical current $j^{(2)}_{\mathrm{pri}} = \sum \alpha_{ijkl} E_{\mathrm{prj}} M_{0k} E_l$. On the other hand, $j^{(2)}_{\mathrm{pri}}$ can be rewritten as the time derivative $\partial_t P^{(2)}_{\mathrm{pri}}$ of the often-used second-order optical polarization $P^{(2)}_{\mathrm{pri}} \propto \sum \chi^{(2)}_{ijl} E_{\mathrm{prj}} E_l$, where $\chi^{(2)}_{ijl}$ is the second-order optical susceptibility. Comparison of these relationships implies $\sum \alpha_{ijkl} M_{0k} \propto \chi^{(2)}_{ijl}$ and $H \propto \chi^{(2)}_{ijl}$ because $H \propto a_{\boldsymbol{E}} M_0 \propto \sum \alpha_{ijkl} M_{0k}$ (Eq. 4).

Implicit pump treatment

Equation 7 demonstrates how the pump fields $\boldsymbol{E}$ and $\boldsymbol{B}$ explicitly modify the linear optical response σ_{ij} of the sample. Alternatively, we can quantify how $\boldsymbol{E}$ and $\boldsymbol{B}$ act on all sample degrees of freedom, which, in turn, modify the σ_{ij} (*23*). To pursue this implicit treatment of the pump, we suppose that $\boldsymbol{E}$ and $\boldsymbol{B}$ affect the optical sample properties exclusively through the electronic spin degrees of freedom. The latter are assumed to be sufficiently characterized by the local sample magnetization $\boldsymbol{M} = \boldsymbol{M}_0 + \Delta\boldsymbol{M}$, where $\Delta\boldsymbol{M}$ arises from the pump action. Thus, we can write $\sigma_{ij} = \sigma_{ij}(\boldsymbol{M})$.

Because we are only interested in changes linear in the pump field, $\sigma_{ij}(\boldsymbol{M})$ still has the symmetry of the sample in the absence of the pump (*23*). Therefore, up to second order in $\boldsymbol{M}$, σ_{ij} acts on the probe field $\boldsymbol{E}_{\mathrm{pr}}$ according to (*46*)

$$\left(\sigma_{ij}\right)(\boldsymbol{M})\boldsymbol{E}_{\mathrm{pr}} = \left(\sigma_{ij}\right)(0)\boldsymbol{E}_{\mathrm{pr}} + a\boldsymbol{M} \times \boldsymbol{E}_{\mathrm{pr}} + b\boldsymbol{M}\left(\boldsymbol{M} \cdot \boldsymbol{E}_{\mathrm{pr}}\right) + c\boldsymbol{M}^2 \boldsymbol{E}_{\mathrm{pr}} \tag{9}$$

Here, $\left(\sigma_{ij}\right)(0)$ is the conductivity in the absence of $\boldsymbol{M}$. The term with coefficient a, b, and c, respectively, indicates MCB, MLB, and an isotropic conductivity change $\propto \boldsymbol{M}^2$, which is not detected (Eq. 6). Combination of Eqs. 6 and 9 yields the pump-induced signal $S \propto \Delta\left[-2aM_z + bM_{\parallel}^2 \sin\left(2\varphi_{\mathrm{pr}} - 2\varphi_{\boldsymbol{M}}\right)\right] + S_{\mathcal{N}}$ and, thus

$$S \propto -a\Delta M_z + b\sin\left(2\varphi_{\mathrm{pr}} - 2\varphi_{\boldsymbol{M}_0}\right) M_0 \Delta M_{\parallel} - b\cos\left(2\varphi_{\mathrm{pr}} - 2\varphi_{\boldsymbol{M}_0}\right) M_0^2 \Delta\varphi_{\boldsymbol{M}} + S_{\mathcal{N}} \tag{10}$$

Here, M_z and $M_{\parallel}$ are the out-of-plane and in-plane components of $\boldsymbol{M}$, and $\varphi_{\boldsymbol{M}}$ is the in-plane angle of $\boldsymbol{M}$ relative to the x axis (Fig. 1B). In the following, we briefly discuss possible $\Delta\boldsymbol{M}$ mechanisms and the non-spin signal contribution $S_{\mathcal{N}}$ (*23*).

Spin-related signal mechanisms

At least three microscopic mechanisms can contribute to a magnetization change $\Delta\boldsymbol{M} = \boldsymbol{M} - \boldsymbol{M}_0$ and, thus, birefringence signal S_{-}.

1) For off-resonant field-like Zeeman torque, $\Delta\boldsymbol{M}$ scales like $\Delta\boldsymbol{M} \propto \boldsymbol{M}_0 \times \boldsymbol{B}$, which is parallel to the z axis and, therefore, yields a MCB-type signal $\propto -aM_0 B\cos\left(\varphi_{\boldsymbol{E}} - \varphi_{\boldsymbol{M}_0}\right)$.

2) Spin accumulation is expected to scale according to $\Delta\boldsymbol{M} \propto \Delta\boldsymbol{s} \propto \boldsymbol{u}_z \times \boldsymbol{E}$, where $\boldsymbol{u}_z$ is the unit vector of the z axis (Fig. 1B). Because of $M_0 \Delta M_{\parallel} = \boldsymbol{M}_0 \cdot \Delta\boldsymbol{M} \propto M_0 E \sin\left(\varphi_{\boldsymbol{M}_0} - \varphi_{\boldsymbol{E}}\right)$ and $M_0^2 \Delta\varphi_{\boldsymbol{M}} = \boldsymbol{u}_z \cdot \left(\boldsymbol{M}_0 \times \Delta\boldsymbol{M}_{\parallel}\right) \propto \boldsymbol{M}_0 \cdot \boldsymbol{E} = M_0 E \cos\left(\varphi_{\boldsymbol{M}_0} - \varphi_{\boldsymbol{E}}\right)$, the signal contribution arises from the two MLB terms in Eq. 10 and writes $\propto bM_0 E\cos\left(2\varphi_{\mathrm{pr}} - \varphi_{\boldsymbol{M}_0} - \varphi_{\boldsymbol{E}}\right)$.

3) For off-resonant field-like spin-orbit torque, we obtain the scaling $\Delta\boldsymbol{M} \propto \boldsymbol{M}_0 \times \Delta\boldsymbol{s} \propto \left(\boldsymbol{M}_0 \cdot \boldsymbol{E}\right)\boldsymbol{u}_z$, and, thus, a MCB-type signal $\propto -aM_0 E\cos\left(\varphi_{\boldsymbol{E}} - \varphi_{\boldsymbol{M}_0}\right)$.

We emphasize that the spin-related signal contributions 1 to 3 are fully consistent with the explicit pump-field treatment in Eq. 8 and, thus, Eq. 2.

Non-spin signals $S_{\mathcal{N}}$

In Eq. 10, the contribution $S_{\mathcal{N}}$ does not arise from $\Delta\boldsymbol{M}$ and rather originates from a pump-induced variation of the non-spin degrees

of freedom $\mathcal{N}$ of the sample (*23*). It depends on geometrical parameters like φ_{M_0} and φ_E in the same way as the *a*, *b*, and *c* terms of Eq. 10.

However, we observe that the rotation and ellipticity component of the measured signal $S_-(t)$ exhibit the same dynamics (fig. S3), consistent with $S_-(t) \propto \Delta M(t)$. In contrast, $S_{\mathcal{N}}$ does not require such identical evolution of probe rotation and ellipticity. Therefore, our signals are most likely dominated by true spin dynamics.

Sample details and characterization

The thin-film stacks are fabricated at room temperature using a Singulus Rotaris magnetron deposition tool with a base pressure of 5×10^{-8} mbar. The metallic layers are grown through DC-magnetron sputtering using targets (diameter, 100 mm) in an Ar gas flow. The sputtering pressure varies from 3 to 6×10^{-3} mbar for the different metallic targets. Substrate cleaning involves sonication in acetone, followed by a similar treatment in isopropanol, and subsequent drying with nitrogen gas flow to eliminate residual organic impurities and acetone.

The terahertz sample conductance is determined by terahertz transmission time-domain spectroscopy (*24*, *36*). For terahertz emission measurements, we use near-infrared pulses (nominal duration 10 fs, center wavelength 800 nm, energy 2.5 nJ) from a Ti:sapphire femtosecond laser oscillator (repetition rate 80 MHz) to excite the metallic FM|HM stacks through the glass substrate in transmission geometry. The emitted terahertz electric field is sampled in a ZnTe(110) electro-optic crystal (thickness 1 mm) by a copropagating femtosecond pulse from the same laser. An external in-plane magnetic field $\boldsymbol{B}_{\text{ext}}$ of magnitude 40 mT saturates layer FM. Emission signals odd in the FM magnetization $\boldsymbol{M}_0$ are measured for each sample by reversing $\boldsymbol{B}_{\text{ext}}$ by 180° and using an equation analogous to Eq. 3. We confirm that all samples are measured in the linear fluence regime with the same pump power under ambient conditions.

Terahertz-pump optical-probe setup

The terahertz-pump optical-probe setup is similar to the one described in (*16*, *19*). To routinely record pump-induced signals at the shot-noise limit of our detection, we use pulses from the Ti:sapphire seed laser of our amplified laser system for probing (*26*) in combination with ZnSe windows placed under Brewster angle behind the sample (*47*).

Terahertz field measurement

To obtain a faithful measurement of the terahertz electric field $\boldsymbol{E}_{\text{inc}}$ incident onto the sample, we use a ferromagnetic Fe(8 nm) thin-film as the ZTD (see fig. S6) (*19*). The measured signal is proportional to the time integral of the driving terahertz magnetic and, thus, electric field. Consequently, in the frequency domain, the transfer function of the ZTD equals

$$\widetilde{H}_{\text{ZTD}}(\omega) = \frac{\widetilde{S}(\omega)}{\widetilde{E}_{\text{inc}}(\omega)} = \frac{a}{\omega} \tag{11}$$

where *a* is a complex-valued coefficient and $\omega/2\pi$ is the frequency. Unlike the STD (Eq. 5), the ZTD response features a pronounced $1/\omega$ low-pass behavior (Eq. 11). However, by sufficiently long signal averaging, the ZTD allows us to access high-frequency signal components up to at least 11 THz as well (*19*).

The only coefficient *a* determining $\widetilde{H}_{\text{ZTD}}(\omega)$ can be obtained by a calibration measurement at a single frequency, thereby providing access to the absolute terahertz field strength. Here, we calibrate our Zeeman detector based on the modeled transfer function of electro-optic sampling in a GaP(110) window (thickness, 50 μm) at frequencies below 2 THz, where the transfer function can be considered frequency-independent (*34*, *35*, *48*). To model GaP, we take an electro-optic coefficient of $r_{41} = -0.88$ pm / V (*49*), a terahertz refractive index of 3.35 (*35*), and a refractive index of 3.19 at the probe wavelength of 800 nm (*50*).

As the ZTD signal is proportional to the vector product $\boldsymbol{M}_0 \times \boldsymbol{B} \propto \boldsymbol{M}_0 \times (\boldsymbol{u}_z \times \boldsymbol{E})$, we use it to precisely calibrate the relative angle between terahertz electric field $\boldsymbol{E}$ and the sample magnetization $\boldsymbol{M}_0$. In this way, we achieve $\boldsymbol{E} \perp \boldsymbol{M}_0$ and minimize the Zeeman torque and spin-orbit torque signals in the STD.

Supplementary Materials

This PDF file includes:

Figs. S1 to S6

References

REFERENCES AND NOTES

1. S. D. Bader, S. S. P. Parkin, Spintronics. *Annu. Rev. Condens. Matter Phys.* **1**, 71–88 (2010).
2. A. Manchon, J. Železný, I. M. Miron, T. Jungwirth, J. Sinova, A. Thiaville, K. Garello, P. Gambardella, Current-induced spin-orbit torques in ferromagnetic and antiferromagnetic systems. *Rev. Mod. Phys.* **91**, 035004 (2019).
3. R. Rouzegar, L. Brandt, L. Nádvorník, D. A. Reiss, A. L. Chekhov, O. Gueckstock, C. in, M. Wolf, T. S. Seifert, P. W. Brouwer, G. Woltersdorf, T. Kampfrath, Laser-induced terahertz spin transport in magnetic nanostructures arises from the same force as ultrafast demagnetization. *Phys. Rev. B* **106**, 144427 (2022).
4. T. Seifert, S. Jaiswal, U. Martens, J. Hannegan, L. Braun, P. Maldonado, F. Freimuth, A. Kronenberg, J. Henrizi, I. Radu, E. Beaurepaire, Y. Mokrousov, P. M. Oppeneer, M. Jourdan, G. Jakob, D. Turchinovich, L. M. Hayden, M. Wolf, M. Münzenberg, M. Kläui, T. Kampfrath, Efficient metallic spintronic emitters of ultrabroadband terahertz radiation. *Nat. Photonics* **10**, 483–488 (2016).
5. T. S. Seifert, L. Cheng, Z. Wei, T. Kampfrath, J. Qi, Spintronic sources of ultrashort terahertz electromagnetic pulses. *Appl. Phys. Lett.* **120**, 180401 (2022).
6. E. T. Papaioannou, R. Beigang, THz spintronic emitters: A review on achievements and future challenges. *Nanophotonics* **10**, 1243–1257 (2021).
7. Z. Feng, H. Qiu, D. Wang, C. Zhang, S. Sun, B. Jin, W. Tan, Spintronic terahertz emitter. *J. Appl. Phys.* **129**, 10901 (2021).
8. T. J. Huisman, T. Rasing, THz emission spectroscopy for THz spintronics. *J. Phys. Soc. Jpn.* **86**, 011009 (2016).
9. L. Cheng, Z. Li, D. Zhao, E. E. M. Chia, Studying spin-charge conversion using terahertz pulses. *APL Mater.* **9**, 70902 (2021).
10. C. Bull, S. M. Hewett, R. Ji, C.-H. Lin, T. Thomson, D. M. Graham, P. W. Nutter, Spintronic terahertz emitters: Status and prospects from a materials perspective. *APL Mater.* **9**, 90701 (2021).
11. W. Wu, C. Y. Ameyaw, M. F. Doty, M. B. Jungfleisch, Principles of spintronic THz emitters. *J. Appl. Phys.* **130**, 91101 (2021).
12. S. Kumar, S. Kumar, Ultrafast terahertz spin and orbital transport in magnetic/nonmagnetic multilayer heterostructures and a perspective. *J. Appl. Phys.* **134**, 170901 (2023).
13. E. T. Papaioannou, G. Torosyan, S. Keller, L. Scheuer, M. Battiato, V. K. Mag-Usara, J. L'huillier, M. Tani, R. Beigang, Efficient terahertz generation using Fe/Pt spintronic emitters pumped at different wavelengths. *IEEE Trans. Magn.* **54**, 1–5 (2018).
14. R. I. Herapath, S. M. Hornett, T. S. Seifert, G. Jakob, M. Kläui, J. Bertolotti, T. Kampfrath, E. Hendry, Impact of pump wavelength on terahertz emission of a cavity-enhanced spintronic trilayer. *Appl. Phys. Lett.* **114**, 041107 (2019).
15. O. Gueckstock, L. Nádvorník, T. S. Seifert, M. Borchert, G. Jakob, G. Schmidt, G. Woltersdorf, M. Kläui, M. Wolf, T. Kampfrath, Modulating the polarization of broadband terahertz pulses from a spintronic emitter at rates up to 10 kHz. *Optica* **8**, 1013–1019 (2021).
16. R. Rouzegar, A. L. Chekhov, Y. Behovitz, B. R. Serrano, M. A. Syskaki, C. H. Lambert, D. Engel, U. Martens, M. Münzenberg, M. Wolf, G. Jakob, M. Kläui, T. S. Seifert, T. Kampfrath, Broadband spintronic terahertz source with peak electric fields exceeding 1.5 MV/cm. *Phys. Rev. Appl.* **19**, 034018 (2023).
17. C. Vicario, C. Ruchert, F. Ardana-Lamas, P. M. Derlet, B. Tudu, J. Luning, C. P. Hauri, Off-resonant magnetization dynamics phase-locked to an intense phase-stable terahertz transient. *Nat. Photonics* **7**, 720–723 (2013).

18. S. Bonetti, M. C. Hoffmann, M.-J. Sher, Z. Chen, S.-H. Yang, M. G. Samant, S. S. P. Parkin, H. A. Dürr, THz-driven ultrafast spin-lattice scattering in amorphous metallic ferromagnets. *Phys. Rev. Lett.* **117**, 087205 (2016).
19. A. L. Chekhov, Y. Behovits, U. Martens, B. R. Serrano, M. Wolf, T. S. Seifert, M. Münzenberg, T. Kampfrath, Broadband spintronic detection of the absolute field strength of terahertz electromagnetic pulses. *Phys. Rev. Appl.* **20**, 034037 (2023).
20. C. Geng, Y. Su, D. Kong, Z. Yang, J. Li, J. Cai, F. Dai, C. Song, X. Wu, Zeeman torque sampling of intense terahertz magnetic field in CoFe. *Opt. Lett.* **49**, 4589–4592 (2024).
21. P. Němec, M. Fiebig, T. Kampfrath, A. V. Kimel, Antiferromagnetic opto-spintronics. *Nat. Phys.* **14**, 229–241 (2018).
22. R. Salikhov, I. Ilyakov, L. Körber, A. Kákay, R. A. Gallardo, A. Ponomaryov, J. C. Deinert, T. V. A. G. de Oliveira, K. Lenz, J. Fassbender, S. Bonetti, O. Hellwig, J. Lindner, S. Kovalev, Coupling of terahertz light with nanometre-wavelength magnon modes via spin–orbit torque. *Nat. Phys.* **19**, 529–535 (2023).
23. Y. Behovits, A. L. Chekhov, S. Y. Bodnar, O. Gueckstock, S. Reimers, Y. Lytvynenko, Y. Skourski, M. Wolf, T. S. Seifert, O. Gomonay, M. Kläui, M. Jourdan, T. Kampfrath, Terahertz Néel spin-orbit torques drive nonlinear magnon dynamics in antiferromagnetic Mn2Au. *Nat. Commun.* **14**, 6038 (2023).
24. O. Gueckstock, L. Nádvorník, M. Gradhand, T. S. Seifert, G. Bierhance, R. Rouzegar, M. Wolf, M. Vafaee, J. Cramer, M. A. Syskaki, G. Woltersdorf, I. Mertig, G. Jakob, M. Kläui, T. Kampfrath, Terahertz spin-to-charge conversion by interfacial skew scattering in metallic bilayers. *Adv. Mater.* **33**, e2006281 (2021).
25. M. Cornet, J. Degert, E. Abraham, E. Freysz, Terahertz Kerr effect in gallium phosphide crystal. *J. Opt. Soc. Am. B* **31**, 1648–1652 (2014).
26. S. F. Maehrlein, I. Radu, P. Maldonado, A. Paarmann, M. Gensch, A. M. Kalashnikova, R. V. Pisarev, M. Wolf, P. M. Oppeneer, J. Barker, T. Kampfrath, Dissecting spin-phonon equilibration in ferrimagnetic insulators by ultrafast lattice excitation. *Sci. Adv.* **4**, eaar5164 (2018).
27. J. Reimann, S. Schlauderer, C. P. Schmid, F. Langer, S. Baierl, K. A. Kokh, O. E. Tereshchenko, A. Kimura, C. Lange, J. Güdde, U. Höfer, R. Huber, Subcycle observation of lightwave-driven Dirac currents in a topological surface band. *Nature* **562**, 396–400 (2018).
28. T. L. Cocker, V. Jelic, R. Hillenbrand, F. A. Hegmann, Nanoscale terahertz scanning probe microscopy. *Nat. Photonics* **15**, 558–569 (2021).
29. T. Kampfrath, K. Tanaka, K. A. Nelson, Resonant and nonresonant control over matter and light by intense terahertz transients. *Nat. Photonics* **7**, 680–690 (2013).
30. H. Y. Hwang, S. Fleischer, N. C. Brandt, B. G. Perkins Jr., M. Liu, K. Fan, A. Sternbach, X. Zhang, R. D. Averitt, K. A. Nelson, A review of non-linear terahertz spectroscopy with ultrashort tabletop-laser pulses. *J. Mod. Opt.* **62**, 1447–1479 (2015).
31. D. Nicoletti, A. Cavalleri, Nonlinear light–matter interaction at terahertz frequencies. *Adv. Opt. Photonics.* **8**, 401–464 (2016).
32. J. A. Fülöp, S. Tzortzakis, T. Kampfrath, Laser-driven strong-field terahertz sources. *Adv. Opt. Mater.* **8**, 1900681 (2020).
33. M. C. Hoffmann, J. A. Fülöp, Intense ultrashort terahertz pulses: Generation and applications. *J. Phys. D. Appl. Phys.* **44**, 083001 (2011).
34. A. Leitenstorfer, S. Hunsche, J. Shah, M. C. Nuss, W. H. Knox, Detectors and sources for ultrabroadband electro-optic sampling: Experiment and theory. *Appl Phys Lett* **74**, 1516–1518 (1999).
35. Q. Wu, X. C. Zhang, 7 terahertz broadband GaP electro-optic sensor. *Appl. Phys. Lett.* **70**, 1784–1786 (1997).
36. T. S. Seifert, N. M. Tran, O. Gueckstock, S. M. Rouzegar, L. Nadvornik, S. Jaiswal, G. Jakob, V. V. Temnov, M. Münzenberg, M. Wolf, M. Kläui, T. Kampfrath, Terahertz spectroscopy for all-optical spintronic characterization of the spin-Hall-effect metals Pt, W and Cu80Ir20. *J. Phys. D Appl. Phys.* **51**, 364003 (2018).
37. K. L. Krewer, W. Zhang, J. Arabski, G. Schmerber, E. Beaurepaire, M. Bonn, D. Turchinovich, Thickness-dependent electron momentum relaxation times in iron films. *Appl. Phys. Lett.* **116**, 102406 (2020).
38. C. M. Saak, E. H. G. Backus, The role of sum-frequency generation spectroscopy in understanding on-surface reactions and dynamics in atmospheric model-systems. *J. Phys. Chem. Lett.* **15**, 4546–4559 (2024).
39. Y. Tong, F. Lapointe, M. Thämer, M. Wolf, R. K. Campen, Hydrophobic water probed experimentally at the gold electrode/aqueous interface. *Angew. Chem. Int. Ed. Engl.* **56**, 4211–4214 (2017).
40. E. R. Eliel, E. W. M. Ham, Q. H. F. Vrehen, G. W. 't Hooft, M. Barmentlo, J. M. Auerhammer, A. F. G. Meer, P. W. van Amersfoort, Studies of interfacial regions by sum-frequency generation with a free-electron laser. *Appl. Phys. A* **60**, 113–119 (1995).
41. H. Yang, G. Ji, M. Choi, S. Park, H. An, H. T. Lee, J. Jeong, Y. D. Park, K. Kim, N. Park, J. Jeong, D. S. Kim, H. R. Park, Suppressed terahertz dynamics of water confined in nanometer gaps. *Sci. Adv.* **10**, adm7315 (2024).
42. Y. Su, J. Le, J. Ma, L. Cheng, Y. Wei, X. Zhai, C. Tian, Probing interface of perovskite oxide using surface-specific terahertz spectroscopy. *Ultrafast Sci.* **3**, 0042 (2023).
43. E. Rongione, S. Fragkos, L. Baringthon, J. Hawecker, E. Xenogiannopoulou, P. Tsipas, C. Song, M. Mičica, J. Mangeney, J. Tignon, T. Boulier, N. Reyren, R. Lebrun, J.-M. George, P. Le Fèvre, S. Dhillon, A. Dimoulas, H. Jaffrès, Ultrafast spin-charge conversion at $SnBi_2Te_4$/Co topological insulator interfaces probed by terahertz emission spectroscopy. *Adv. Opt. Mater.* **10**, 2102061 (2022).
44. C. Ciccarelli, L. Anderson, V. Tshitoyan, A. J. Ferguson, F. Gerhard, C. Gould, L. W. Molenkamp, J. Gayles, J. Železný, L. Šmejkal, Z. Yuan, J. Sinova, F. Freimuth, T. Jungwirth, Room-temperature spin–orbit torque in NiMnSb. *Nat. Phys.* **12**, 855–860 (2016).
45. J. A. Krieger, S. Stolz, I. Robredo, K. Manna, E. C. McFarlane, M. Date, B. Pal, J. Yang, E. B. Guedes, J. H. Dil, C. M. Polley, M. Leandersson, C. Shekhar, H. Borrmann, Q. Yang, M. Lin, V. N. Strocov, M. Caputo, M. D. Watson, T. K. Kim, C. Cacho, F. Mazzola, J. Fujii, I. Vobornik, S. S. P. Parkin, B. Bradlyn, C. Felser, M. G. Vergniory, N. B. M. Schröter, Weyl spin-momentum locking in a chiral topological semimetal. *Nat. Commun.* **15**, 3720 (2024).
46. L. Nádvorník, M. Borchert, L. Brandt, R. Schlitz, K. A. de Mare, K. Výborný, I. Mertig, G. Jakob, M. Kläui, S. T. B. Goennenwein, M. Wolf, G. Woltersdorf, T. Kampfrath, Broadband terahertz probes of anisotropic magnetoresistance disentangle extrinsic and intrinsic contributions. *Phys. Rev. X* **11**, 021030 (2021).
47. S. Ahmed, J. Savolainen, P. Hamm, Detectivity enhancement in THz electrooptical sampling. *Rev. Sci. Instrum.* **85**, 013114 (2014).
48. T. Kampfrath, J. Nötzold, M. Wolf, Sampling of broadband terahertz pulses with thick electro-optic crystals. *Appl. Phys. Lett.* **90**, 231113 (2007).
49. Y. Berozashvili, S. Machavariani, A. Natsvlishvili, A. Chirakadze, Dispersion of the linear electro-optic coefficients and the non-linear susceptibility in GaP. *J. Phys. D. Appl. Phys.* **22**, 682–686 (1989).
50. D. E. Aspnes, A. A. Studna, Dielectric functions and optical parameters of Si, Ge, GaP, GaAs, GaSb, InP, InAs, and InSb from 1.5 to 6.0 eV. *Phys. Rev. B.* **27**, 985 (1983).
51. M. C. Hoffmann, N. C. Brandt, H. Y. Hwang, K.-L. Yeh, K. A. Nelson, Terahertz Kerr effect. *Appl. Phys. Lett.* **95**, 231105 (2009).
52. M. Sajadi, M. Wolf, T. Kampfrath, Terahertz-field-induced optical birefringence in common window and substrate materials. *Opt. Express* **23**, 28985–28992 (2015).
53. A. L. Chekhov, Y. Behovits, J. J. F. Heitz, C. Denker, D. A. Reiss, M. Wolf, M. Weinelt, P. W. Brouwer, M. Münzenberg, T. Kampfrath, Ultrafast demagnetization of iron induced by optical versus terahertz pulses. *Phys. Rev. X* **11**, 041055 (2021).

Acknowledgments: We are grateful to L. Nadvorník for contributions during the early stage of this work and to P. M. Oppeneer for fruitful discussions. **Funding:** We acknowledge funding by the DFG Collaborative Research Center SFB TRR 227 "Ultrafast spin dynamics" (project ID 328545488, projects A05 and B02), the DFG Priority Program SPP2314 INTEREST (project ITISA), the DFG Collaborative Research Center SFB TRR 173 "Spin+X" (project ID 268565370, projects A01, B02), the DFG Major Research Instrumentation grant no. INST 130/1268-1 FUGG, the FET Open grant no. 863155 (s-Nebula), the ERC-2023 Advanced Grant ORBITERA (grant no. 101142285), ERC-2019-SyG 3D MAGiC (grant no. 856538), and MSCA ITN MagnEfi (grant no. 860060). S.J. acknowledges funding from The Marie-Curie Seventh Framework program—ITN "WALL" (grant no. 608031). **Author contributions:** Conceptualization: A.L.C., T.K., T.S.S., J.J.F.H., M.M., M.W., and M.K. Methodology: A.L.C., Y.B., T.K., J.J.F.H., and M.M. Supervision: T.K., A.L.C., M.M., and M.K. Investigation: A.L.C., Y.B., O.G., J.J.F.H., B.R.S., and A.R. Resources: M.-A.S., S.J., B.R.S., G.J., M.K., M.M., and J.K. Writing—original draft: A.L.C. and T.K. Writing—review and editing: T.K., Y.B., G.J., M.K., M.M., T.S.S., and M.W. Project administration: T.K., M.M., and M.K. Funding acquisition: T.K., M.W., and M.K. Visualization: A.L.C., T.K., and G.J. Formal analysis: O.G., Y.B., A.L.C., and J.J.F.H. Validation: A.L.C., Y.B., and G.J. Software: A.L.C., Y.B., and J.J.F.H. **Competing interests:** T.S.S. and T.K. are shareholders of TeraSpinTec GmbH, and T.S.S. is an employee of TeraSpinTec GmbH. The authors declare that they have no other competing interests. **Data and materials availability:** All data needed to evaluate the conclusions in the paper are present in the paper and/or the Supplementary Materials.

Submitted 30 May 2024
Accepted 13 February 2025
Published 21 March 2025
10.1126/sciadv.adq7741